Supplemental Information: Anomalous thermal transport across the superionic transition in ice

Rong Qiu,[1,2] Qiyu Zeng,[1,2] Han Wang,[3] Dongdong Kang,[1,2] Xiaoxiang Yu,[1,2,*] and Jiayu Dai[1,2,†]

[1] *Department of Physics, National University of Defense Technology, Changsha 410073, China*
[2] *Hunan Key Laboratory of Extreme Matter and Applications, National University of Defense Technology, Changsha 410073, China*
[3] *Laboratory of Computational Physics, Institute of Applied Physics and Computational Mathematics, Beijing 100088, China*

(Dated: October 27, 2023)

I. GREEN-KUBO METHOD FOR THERMAL CONDUCTIVITY

With DPMD simulation, the lattice thermal conductivity κ is obtained from the integral of the heat current auto correlation function (HCACF), known as Green–Kubo formula [1, 2],

$$\kappa_{\alpha\beta} = \frac{V}{k_{\mathrm{B}} T_i^2} \int_0^{\infty} \langle J_\alpha(0) J_\beta(t_{corre}) \rangle dt_{corre} \tag{1}$$

where $\kappa_{\alpha\beta}$ is the $\alpha\beta^{th}$ component of the thermal conductivity tensor, V is the volume of the material system, k_B is the Boltzmann constant, T_i is the lattice temperature, t_{corre} is the heat current autocorrelation time, and J_α is the α-th component of the full heat current vector $\mathbf{J}$, which is typically computed as [3],

$$\mathbf{J} = \frac{1}{V}(\sum_i \mathbf{v}_i \epsilon_i + \sum_i \Xi_i \cdot \mathbf{v}_i) \tag{2}$$

Here, $\mathbf{v}_i$, ϵ_i and Ξ_i are the velocity, energy and stress tensor of atom i respectively.

The decomposition of heat current into a heat conduction term and a heat convection term can provide insights into the mechanism behind the abnormal trend of κ [4],

$$\mathbf{J}_{cond} = \frac{1}{V} \sum_i \Xi_i \cdot \mathbf{v}_i \tag{3}$$

$$\mathbf{J}_{conv} = \frac{1}{V} \sum_i \mathbf{v}_i \epsilon_i \tag{4}$$

these decomposition results in three contribution to total thermal conductivity: conduction-conduction correlation, convection-convection correlation, and convection-conduction correlation, denoted as κ_{cond}, κ_{conv}, and κ_{cross} respectively. In the manuscript, we mainly focus on the first two terms to unravel the contribution from collective modes and proton diffusion.

II. COMPUTATIONAL DETAILS

To train the DP model, training sets are collected from previous work [5], where the high-pressure ice-VII and ice-VII" are sampled across wide thermodynamic condition ($200 \leq T \leq 2400$ K, $1 \leq P \leq 50$ GPa). The superionic phase transition boundaries are well captured by the generated DP model.

For DP training, the embedding network is composed of three layers (25, 50, and 100 nodes) while the fitting network has three hidden layers with 240 nodes in each layer. The radius cutoff r_c is chosen to be 6.0 Å. The total number of training steps is set to 8,000,000. The weight parameters in loss function for energies p_e, forces p_f, and virials p_V are set to $(0.02, 1000.0, 2.0)$ at the beginning of training and gradually change to $(1.0, 1.0, 1.0)$.

The accuracy of generated DP model is tested along the isobar of 30 GPa (T = 400, 800, 1200, 1600, 2000 K), covering static and super ionic phase. The prediction errors are shown in Fig.S1, where the root mean square error

* Corresponding author: xxyu@nudt.edu.cn
† Corresponding author: jydai@nudt.edu.cn

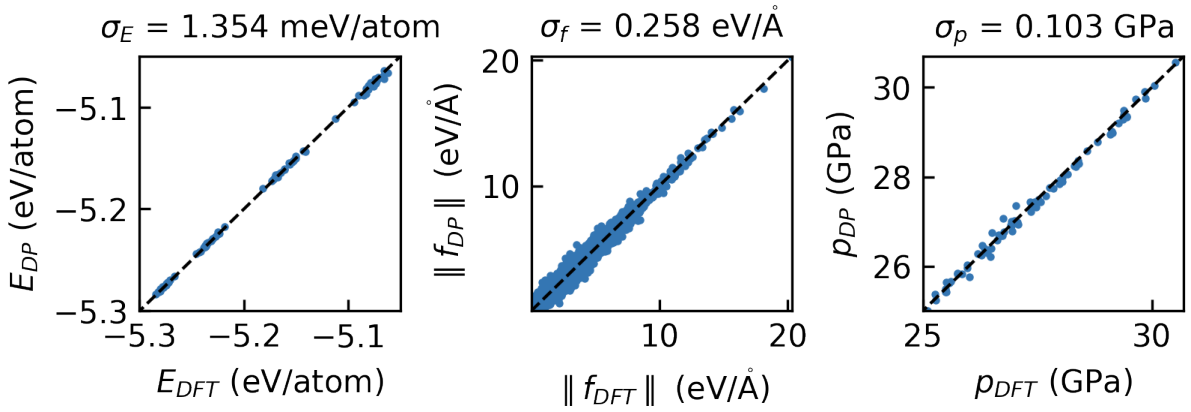

Figure S1. Parity plot of DP-predicted and DFT-calculated energies, forces, and pressures along isobar of 30 GPa

(RMSE) of energy σ_E is 1.354 meV/atom, the RMSE of forces σ_f is 0.258 eV/Å, and the RMSE of pressure σ_p is 0.103 GPa.

DPMD simulations were performed with the LAMMPS package [3] combining with USER-DEEPMD modules [6]. The timestep was set to 0.5 fs and the Nosé-Hoover thermostat [7, 8] was employed in the isothermal ensemble. For each (P,T) case, the equilibrium lattice constant is firstly obtained under NPT ensemble with 1296 atoms. Then the simulation box is fixed to maintain the pressure of 30 Gpa in the following simulation. After a thermalization stage of 20 ps under NVT ensemble, the ensemble is switched into the NVE ensemble to calculate the HCACF during the next 220 ps with the correlation time set to 22 ps. Each (P,T) case repeats 20 times, with independent initial velocity distribution to provide a representative sample for the relevant statistical analysis. In general, each (P,T) case requires a total calculation of 4.8 ns of MD trajectory.

Supercells containing 48, 384, 1296, 3072 atoms were used to find out converged simulation size for removal of size effect. The thermodynamic condition of p = 30 GPa, T = 1400 K is chosen due to a relatively higher thermal conductivity. From the convergence of κ presented in Fig.S2, we chose the 1296-atom-supercell to further conduct a series of DPMD simulations.

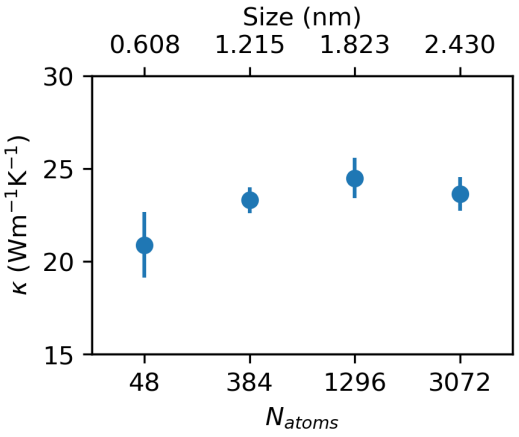

Figure S2. Size dependence of thermal conductivity at thermodynamic condition of (p = 30 GPa, T = 1400 K).

The normalized HCACF and integrated HCACF (also known as cumulative thermal conductivity) are presented in Fig. 1. Since the ice-VII and ice-VII" are isotropic, all results are averaged over x, y, z directions. We can observe that the normalized HCACF decreases from unity to 10^{-3} within t = 1 ps, resulting in fast convergence of thermal conductivity. Furthermore, we observe pronounced fluctuations in the cumulative thermal conductivity during each individual simulation, especially under high temperatures. Therefore, conducting 20 individual simulations can provide more statistically reliable results. The thermal conductivity is then obtained by averaging the ensemble-

averaged integrated HCACF over the time interval of [10, 20] ps.

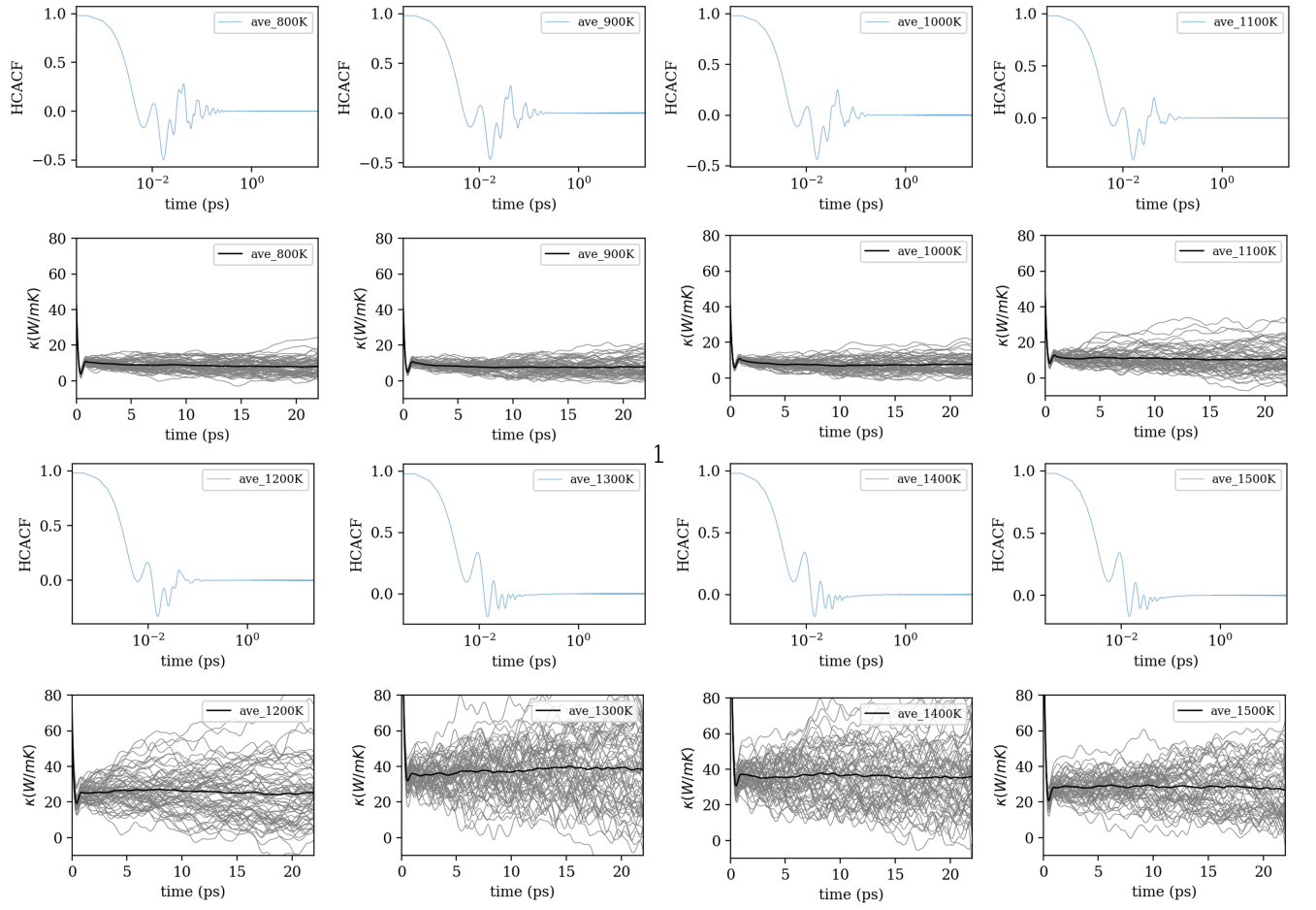

Figure S3. The normalized heat-current auto-correlation function of several (p,T) cases, and the integrated HCACF.

III. PROTON DIFFUSION IN ICE-VII AND ICE-VII"

To investigate the proton transfer dynamics and highlight the superionic phase transition, we generated 20-ps-long trajectories for hydrogen and oxygen atoms at different temperatures, as shown in Fig.S4. At T = 800 K, the delocalization of hydrogen atom is not observed. At T = 1000 K, the proton can hop within the half-diagonal O-H···O bonds. With a higher thermal kinetic energy (T = 1200 k), protons can migrate from an O-H···O bond to another, leading to a fast change in the orientation of water molecules. Across the superionic phase transition, the delocalization of protons changes significantly. The proton diffuse fastly out of the bcc oxygen sub-lattice.

To obtain the diffusion coefficient, the mean-square-displacement (MSD) of hydrogen and oxygen atoms were calculated according to

$$D = \frac{1}{6t}\langle|\mathbf{R}_i(t) - \mathbf{R}_i(0)|^2\rangle$$

where the $\mathbf{R}_i$ is the position of the ith particle.

As shown in Fig.S5, the values of MSD were estimated with 10-ps-long trajectories, averaged by 50 individual simulation runs. We can clearly identify the onset of hydrogen diffusion at T = 1000 K, characterized by the linear time dependence of MSD. As temperature increases, the hydrogen diffusion is enhanced significantly while the oxygen atoms only vibrate around the equilibrium position even up to T = 1500 K.

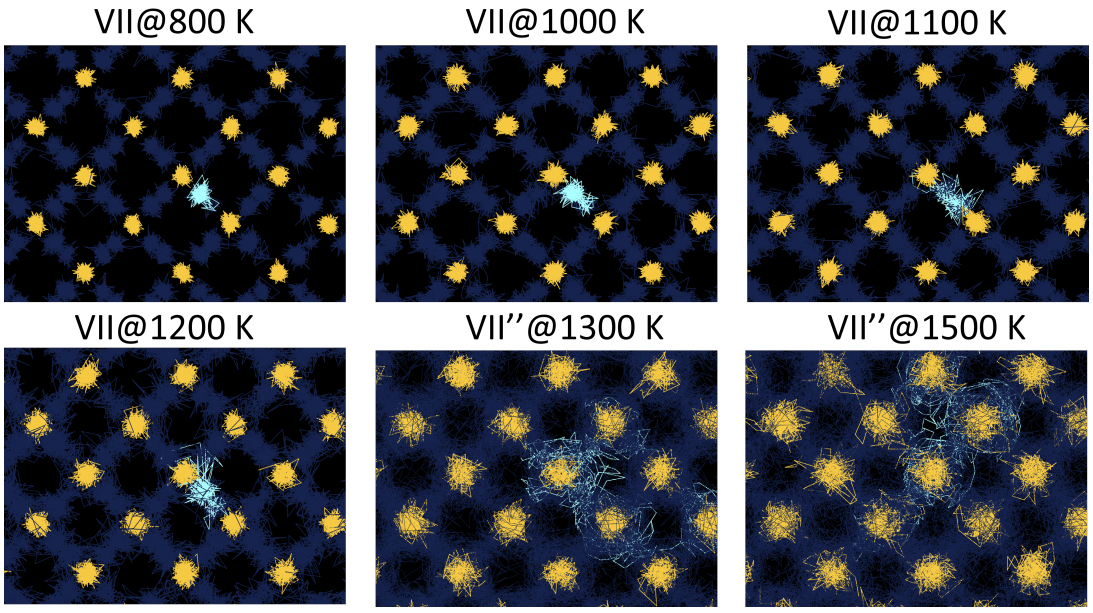

Figure S4. Atomic trajectories of ice VII and VII" at different temperatures during a 20-ps long run. The oxygen and hydrogen atoms trajectories are marked orange and dark blue respectively. The cyan color is used to highlight the selected hydrogen atoms that undergo transitions from bonded states between two adjacent oxygen atoms to superionic states around different oxygen atoms

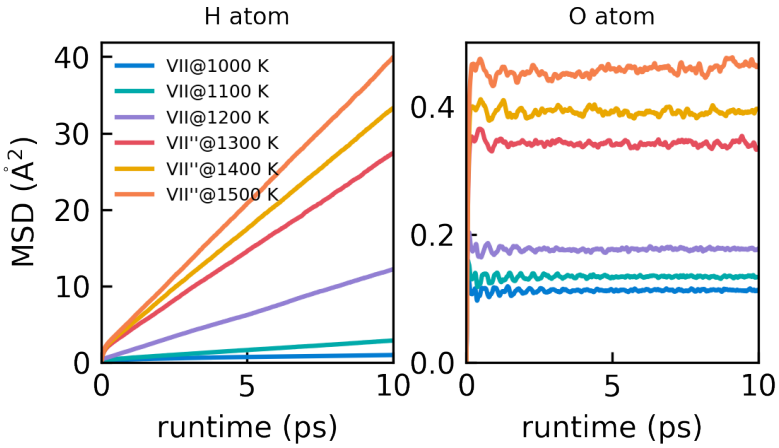

Figure S5. MSD of (left) hydrogen and (right) oxygen atoms at different temperatures along the isobar of p = 30 GPa. All curves are ensemble-averaged results, estimated from 50 individual simulations with different initial velocity distributions.

IV. COLLECTIVE DYNAMICS

The molecular dynamics trajectories allows to further understand the collective behavior across superionic phase transition. The spectrum of density-density correlation is first investigated, known as dynamic structure factor (DSF),

$$S(\mathbf{k},\omega) = \frac{1}{2\pi}\int_{-\infty}^{\infty}\frac{1}{N}\langle\rho(\mathbf{k},t)\rho(-\mathbf{k},0)\rangle e^{i\omega t}dt$$
$$= \frac{1}{2\pi NT}|\rho(\mathbf{k},\omega)|^2 \tag{5}$$

where $\rho(k,t)$ the the Fourier transform of the time-dependent density $\rho(\mathbf{r},t)$ in real space for a period of T. Here we paid special attention to the central peak, which encodes the thermal diffusion process as wavenumber is small enough

to reach the hydrodynamic regime [4]. At the hydrodynamic limit, the shape of this central peak can be described by a Lorentzian function with peak width relating to the ionic thermal diffusivity $D_T = \kappa/\rho c_p$, gives

$$S(k,\omega) \propto 2D_T k^2/(\omega^2 + (D_T k^2)^2) \tag{6}$$

Here we run 150-ps-long trajectories under NVT ensemble to have a better frequency resolution according to $\Delta\omega = 2\pi/T = 0.041$ THz. By estimating density-fluctuation correlation of hydrogen density ρ_H and oxygen density ρ_O, we can obtain the DSF contributed by hydrogen and oxygen respectively.

Then, the DSF at smallest wavenumber is fitted to hydrodynamic formula,

$$\begin{aligned} S(k,\omega) = \frac{S(k)}{2\pi}[(\frac{\gamma-1}{\gamma})\frac{2D_T k^2}{\omega^2 + (D_T k^2)^2} \\ + \frac{1}{\gamma}(\frac{\Gamma k^2}{(\omega + c_s k^2)^2 + (\Gamma k^2)^2} + \frac{\Gamma k^2}{(\omega - c_s k^2)^2 + (\Gamma k^2)^2})] \end{aligned} \tag{7}$$

where $D_T = \kappa/\rho c_p$ is ionic thermal diffusivity, with κ the ionic thermal conductivity. c_s is the adiabatic speed of sound, Γ is the sound attenuation constant, and $\gamma = c_p/c_V$ is the ratio of the heat capacity at constant pressure c_p to the heat capacity at constant volume c_V.

From Fig.S6, we can see the $S(k,\omega)$ forms well-defined Rayleigh-Brillouin triplet, and the width of the zero-frequency peak is inverse to the thermal diffusion D_T. By fitting the DPMD-estimated $S(k,\omega)$, we present hydrodynamic curves at different temperatures in the manuscript to highlight the different thermal diffusive process experienced by the diffusive proton and oxygen sub-lattice.

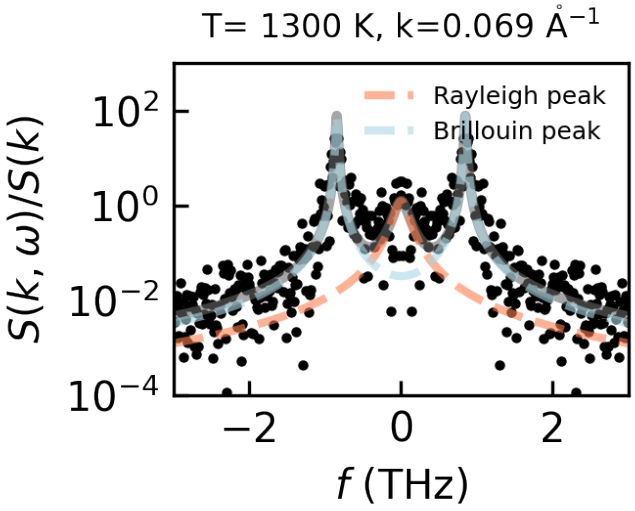

Figure S6. dynamic structure factor of ice-VII" at p = 30 GPa, T = 1300 K. The black dots denot the DPMD results estimated from 150-ps-long trajectories. The gray lines denotes the hydrodynamic fitting curve, where the red and lightblue dashed line represent the contribution of Rayleigh peak and Brillouin peak.

To understand the heat conduction, the current correlation spectra $C(k,\omega)$ is calculated from 50-ps-long molecular dynamics trajectories with a large supercell containing 6,480 atoms ($L_x = 5L_y = 5L_z$) by extracting microscopic current spatial-temporal correlation,

$$C(\mathbf{k},\omega) = \frac{1}{NT}\sum_{\alpha}\sum_{b}^{N_b} m_b |\int_{-\infty}^{\infty} j_\alpha(\mathbf{k},t)e^{i\omega t}dt|^2 \tag{8}$$

$$j_\alpha(\mathbf{k},t) = \sum_i v_{i,\alpha}(t)e^{i\mathbf{k}\cdot\mathbf{r}_i(t)} \tag{9}$$

where $j_\alpha(\mathbf{k},t)$ the Fourier component of microscopic particle current, which can be separated into longitudinal and transverse parts being parallel and perpendicular to the wavevector, and $u_{i,\alpha}$ is the velocity of particle i along α

direction. Considering the ice-VII and ice-VII" is cubic supercell, only the wavevector $\mathbf{k} = (n_x\Delta k, 0, 0)$ along x-direction is considered.

The $C(\mathbf{k}, \omega)$ is the spectrum of current-current correlation function weighted by element mass, also known as spectral energy density (SED), providing full information of collective modes (group velocity, lifetime) inside the complex ice polymorph with taking care of the anharmonicity to all orders inherently.

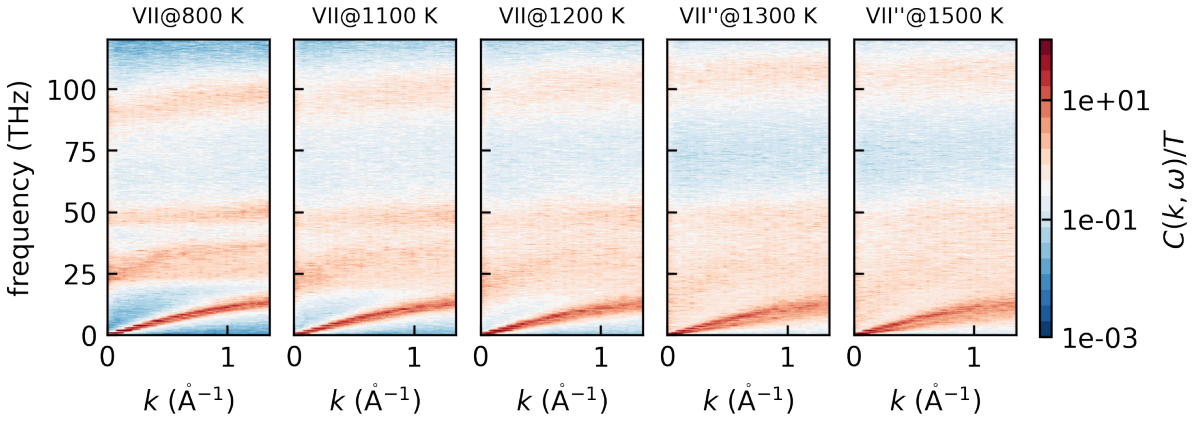

Figure S7. Normalized spectra energy density $C(k, \omega)$, where the direction of wavevector $\mathbf{k} = (n_x\Delta k_x, 0, 0)$ is set to x direction with the wavenumber resolution of $\Delta k_x = 2\pi/L_x \sim 0.07$ Å^{-1}.

From Fig.S7, the SEDs in full frequency regime are presented, which can be classified into four types of collective motion, corresponding to hydrogen bond bending and stretching mode (HB/HS, $0 \leq \omega/2\pi \leq 20$ THz), molecular libration mode (L, $20 \leq \omega/2\pi \leq 30$ THz), molecular bending mode (B, $40 \leq \omega/2\pi \leq 50$ THz), and molecular stretching mode (S, $70 \leq \omega/2\pi \leq 120$ THz).

As temperature increases, all the collective mode broadens, indicating a stronger phonon scattering process under high temperatures. Most phonon branch experiences decrease in frequency, except the O-H stretching mode that exhibits a hardening upon temperature. Across the superionic phase transition, the broadening of acoustic and optical mode is significant, making the O-H libration and bending mode indistinguishable.

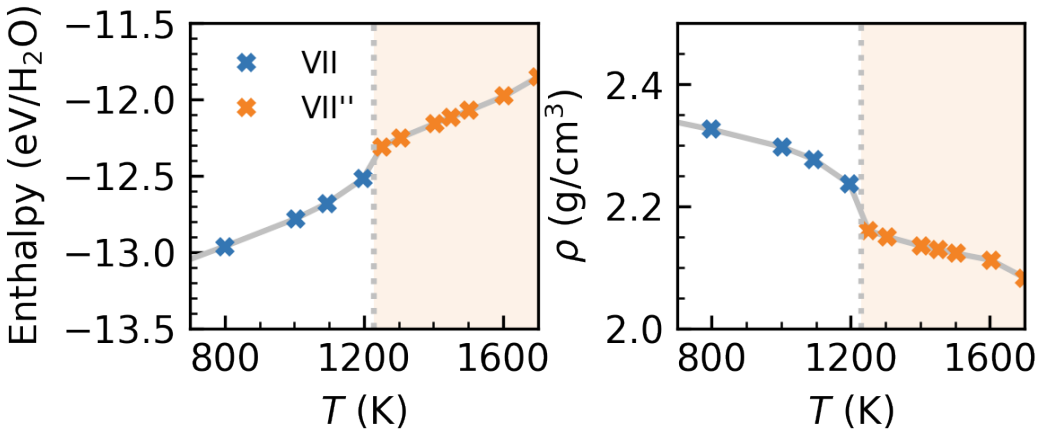

Figure S8. (left) enthalpy and (right) density of ice along isobar of p = 30 GPa, the dashed line denotes the superionic phase transition.

V. THERMODYNAMIC PROPERTIES ACROSS SUPERIONIC TRANSITION

here we present the enthalpy and density of ice along the isobar of p = 30 GPa in the Fig.S8. The enthalpy exhibits a sharp increase acrossn as temperature increase above 1200 K, which is consistent with previous DPMD simulation [5]. The density across superionic phase transition also exhibits a sharp decrease from 2.23 g/cm^3 to 2.16 g/cm^3. The above discontinuities indicates a weakly first-order phase transition, where volume expansion and absorption of latent heat is expected.

[1] M. S. Green, Markoff random processes and the statistical mechanics of time-dependent phenomena, J. Chem. Phys. **20**, 1281 (1952).
[2] R. Kubo, Statistical-mechanical theory of irreversible processes. i. general theory and simple applications to magnetic and conduction problems, Journal of the Physical Society of Japan **12**, 570 (1957).
[3] S. Plimpton, Fast parallel algorithms for short-range molecular dynamics, Journal of computational physics **117**, 1 (1995).
[4] Q. Zeng, X. Yu, Y. Yao, T. Gao, B. Chen, S. Zhang, D. Kang, H. Wang, and J. Dai, Ab initio validation on the connection between atomistic and hydrodynamic description to unravel the ion dynamics of warm dense matter, Phys. Rev. Research **3**, 033116 (2021).
[5] L. Zhang, H. Wang, R. Car, and W. E, Phase diagram of a deep potential water model, Phys. Rev. Lett. **126**, 236001 (2021).
[6] H. Wang, L. Zhang, J. Han, and E. Weinan, Deepmd-kit: A deep learning package for many-body potential energy representation and molecular dynamics, Computer Physics Communications **228**, 178 (2018).
[7] S. Nosé, A unified formulation of the constant temperature molecular dynamics methods, J. Chem. Phys. **81**, 511 (1984).
[8] W. G. Hoover, Canonical dynamics: Equilibrium phase-space distributions, Phys. Rev. A **31**, 1695 (1985).